Journal of Power Sources 674 (2026) 239758

Contents lists available at ScienceDirect

Journal of Power Sources

journal homepage: www.elsevier.com/locate/jpowsour

Unraveling activity-durability trade-off in coated Fe-N-C catalysts for oxygen reduction via pyrolysis-duration-driven structural evolution

Li Jiao [a,*], Geunsu Bae [b], Nicolas Donzel [a], Marc Dupont [a], Frédéric Lecoeur [a], Min Wook Noh [b], Anastassiya Khan [d], Andrea Zitolo [d], Laetitia Dubau [e], Goran Dražić [f], Chang Hyuck Choi [b,c,**], Frédéric Jaouen [a,***]

[a] ICGM, Univ. Montpellier, CNRS, ENSCM, Montpellier, 34293, France
[b] Department of Chemistry, Pohang University of Science and Technology, Pohang, 37673, Republic of Korea
[c] Institute for Convergence Research and Education in Advanced Technology, Yonsei University, Seoul, 03722, Republic of Korea
[d] Synchrotron SOLEIL, L'orme des Merisiers, Saint Aubin, Gif-sur-Yvette, BP 48, France
[e] University of Grenoble Alpes, University of Savoie Mont Blanc, CNRS, Grenoble INP, LEPMI, Grenoble, France
[f] Department of Materials Chemistry, National Institute of Chemistry, Ljubljana, Slovenia

HIGHLIGHTS

- Quantitative tracking of Fe-N_4 site evolution during CVD and its impact.
- In situ DEMS reveals improved corrosion resistance of coated carbon surface.
- TG-MS identifies ZIF-8 decomposition species, clarifying coating chemistry.

GRAPHICAL ABSTRACT

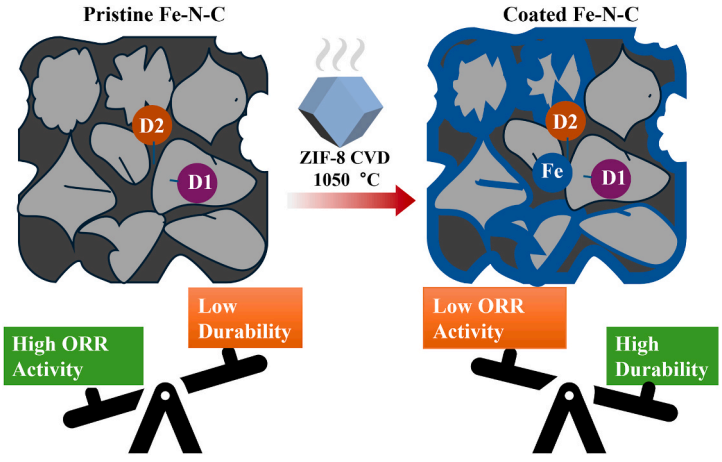

ARTICLE INFO

Keywords:
Oxygen reduction
Chemical vapor deposition
Iron-nitrogen-carbon
Stability

ABSTRACT

Fe-N-C catalysts stand out among precious-metal-free materials for the oxygen reduction reaction (ORR), yet their durability in acidic environments remains a critical challenge. The degradation pathways, particularly following high-temperature post-treatments, are not fully understood. In this study, we coated a benchmark Fe-N-C catalyst via chemical vapor deposition (CVD) using Zeolitic Imidazolate Framework-8 (ZIF-8), with dwell times ranging from 1 to 10 h at 1050 °C to tune the catalyst structure. During CVD process, a fraction of the Fe-N_4

* Corresponding author.
** Corresponding author. Department of Chemistry, Pohang University of Science and Technology, Pohang, 37673, Republic of Korea.
*** Corresponding author.
E-mail addresses: li.jiao@umontpellier.fr (L. Jiao), chchoi@postech.ac.kr (C.H. Choi), frederic.jaouen@umontpellier.fr (F. Jaouen).

https://doi.org/10.1016/j.jpowsour.2026.239758
Received 27 August 2025; Received in revised form 16 February 2026; Accepted 26 February 2026
Available online 6 March 2026

sites was transformed into Fe nanoparticles due to the reducing environment created by volatile species derived from ZIF-8. This leads to decreased Fe-N_4 site density and turnover frequency, both contributing to decreased ORR activity. However, improved durability is observed, and can be explained in part by promoted graphitization catalyzed by Fe particles during pyrolysis. We reveal with online differential electrochemical mass spectrometry that CVD with ZIF-8 leads to strongly reduced carbon corrosion, an effect not observed when applying the same annealing treatment but without ZIF-8, supporting the deposition of a N-doped carbon coating in the former case. The study also reports the complex effect of CVD duration on activity, site density, turnover frequency and durability. Overall, these findings highlight the structural effects on ORR activity and durability of Fe-N-C catalysts, providing valuable insights for designing more robust Fe-N-C catalysts.

1. Introduction

The global push toward decarbonization has placed electrochemical energy technologies, particularly proton exchange membrane fuel cells (PEMFCs), at the forefront of sustainable transportation due to their high energy conversion efficiency and low CO_2 emissions. However, large-scale deployment of PEMFCs is hindered by their reliance on costly and scarce precious-group metal (PGM) catalysts, specifically platinum (Pt), for the kinetically sluggish oxygen reduction reaction (ORR) at the cathode [1]. Among PGM-free alternatives, catalysts based on atomically dispersed nitrogen-coordinated iron sites (Fe-N_4) embedded within porous carbon matrices (Fe-N-C) have emerged as the most promising candidates [2–6]. These catalysts have demonstrated ORR activities approaching those of Pt/C under specific conditions, particularly in H_2/O_2 PEMFCs [7,8]. However, a key limitation is their insufficient long-term durability, typically arising from Fe site demetallation, carbon matrix corrosion or both under acidic fuel cell operating conditions [9–15].

Addressing this challenge requires a deeper understanding of the structure-property relationships that govern degradation. Mössbauer spectroscopy has revealed the presence of two primary types of Fe-N_4 sites: a high-spin FeN_4C_{12} species (referred to as D1), which is more active but less stable, and a low-spin FeN_4C_{10} species (referred to as D2), which is more resistant to degradation during ORR [2,16–18]. Increasing the D2/D1 ratio has been proposed as a strategy to improve catalyst stability. A recent study has shown that coating Fe-N-C catalysts with a thin N-doped carbon layer via chemical vapor deposition (CVD) using a Zeolitic imidazolate framework (ZIF-8) precursor markedly improves durability [19]. ZIF-8 starts decomposing only at ~600 °C, which allows its efficient utilization to form a carbon coating layer at 750–1000 °C [20]. The improvement has been credited to the partial transformation of D1 into D2 sites, supported by an increase in the D2/D1 ratio from 0.44 (uncoated) catalyst to 0.79 (coated), as estimated by Mössbauer spectroscopy at room temperature [19]. Other work has reported a similar increase in the D2/D1 ratio from 0.59 to 1.49 when pyrolysis was conducted in 10% H_2/90% Ar rather than in pure Ar, suggesting that reductive environments promote the transformation of disordered carbon into more ordered carbon (associated with FeN_4C_{12}), thus favoring the stabilization of more graphitic FeN_4C_{10} sites [21]. Improvements in stability, accompanied by increased D2/D1 ratio and graphitization, have also been observed in catalysts pyrolyzed at 1200 °C compared to 900–1100 °C [22,23]. Despite these advances, it remains unclear whether enhanced durability stems primarily from selective stabilization of Fe-N_4 sites, enhanced graphitization, or suppressed carbon corrosion, especially considering the complex structural changes that occur during high-temperature post-treatment. Moreover, the effects of CVD process parameters, such as dwell time, on Fe site retention and carbon matrix evolution have not been systematically investigated. The thermal evolution of both ZIF-8 and the parent catalyst during CVD, which likely governs the formation of the carbon coating layer, also remains unexplored.

In this work, we investigate how the thermal decomposition of ZIF-8 during CVD influences the structure, ORR activity, and durability of Fe-N-C catalysts. By varying the dwell time of CVD at 1050 °C (1–10 h), we tracked the transformation of Fe-N_4 sites, the formation of Fe nanoparticles, and changes in graphitization using a suite of techniques, including Mössbauer spectroscopy, X-ray absorption spectroscopy (XAS), scanning transmission electron microscopy (STEM), and differential electrochemical mass spectroscopy (DEMS). We demonstrate that prolonged CVD reduces Fe-N_4 sites and ORR activity, but enhances durability by passivating the carbon surface and suppressing carbon corrosion, rather than stabilizing Fe-N_4 sites. These results provide fundamental insight into degradation mechanisms and offer practical guidelines for designing robust, high-performing PGM-free catalysts for PEMFCs.

2. Results

2.1. Fe-N-C catalyst synthesis and structural characterization

The Fe-N-C catalyst (labeled as $Fe_{0.5}NH_3$) was synthesized via a two-step pyrolysis of a ball-milled mixture of laboratory-synthesized ZIF-8 (~80 nm), 1,10-phenanthroline, and iron (II) acetate. The mixture was first pyrolyzed under argon flow at 1050 °C with a heating rate of 5 °C·min^{-1}, and held at 1050 °C for 1 h, followed by a flash pyrolysis of 5 min under ammonia flow at 950 °C, following our previously reported method [2]. See Experimental Methods section for further details of the $Fe_{0.5}NH_3$ synthesis.

Transmission electron microscopy (TEM), Fe K-edge XAS and ^{57}Fe Mössbauer spectroscopy collectively confirmed the exclusive presence of atomically dispersed Fe-N_4 sites within a porous carbon matrix (Fig. S1). This atomic dispersion was further supported by the single Fe-N/O peak at 1.4 Å observed in the Fourier-transformed extended X-ray absorption fine structure (FT-EXAFS) spectrum (Fig. S1). N_2 sorption analysis revealed a Brunauer-Emmett-Teller (BET) surface area of 813 m^2 g^{-1} and a microporous surface area (derived from NLDFT analysis of the full adsorption isotherm) of 875 m^2 g^{-1} (Fig. S2), indicating high porosity. Note that BET analysis is not strictly applicable to highly microporous materials, explaining the apparent above discrepancy of a total specific area being lower than a microporous area. The BET area is herein only used to concisely summarise trends in specific areas of the materials. X-ray diffraction (XRD) pattern exhibited a broad (002) reflection centered at ~20.6°, which is significantly lower than the graphitic peak at 26.0°, indicating a disordered carbon structure with expanded interlayer spacing (Fig. S2).

To modify the surface structure, $Fe_{0.5}NH_3$ was coated via CVD using ZIF-8 as a precursor. The ZIF-8 powder was placed upstream of the $Fe_{0.5}NH_3$ under Ar flow, and pyrolyzed at 1050 °C for 1, 4, or 10 h. The resultant coated samples are labeled as C_Fe_*x*, where *x* refers to the dwell time. These CVD-treated catalysts showed a notable decrease in microporosity and a slight increase in mesopore content, with BET surface areas dropping to ~450 m^2 g^{-1} for C_Fe_4 and C_Fe_10 (Fig. S2). This is attributed to the increased graphitization, as evidenced by a sharper (002) XRD peak at ~26.0° (Fig. S2). High-resolution TEM (Fig. 1a–c) revealed increasing long-range graphitic order with longer CVD durations. While $Fe_{0.5}NH_3$ only showed short-range order, C_Fe_1 and C_Fe_10 displayed progressively more well-defined graphitic domains. A control sample (B_Fe_10) was prepared by pyrolyzing $Fe_{0.5}NH_3$

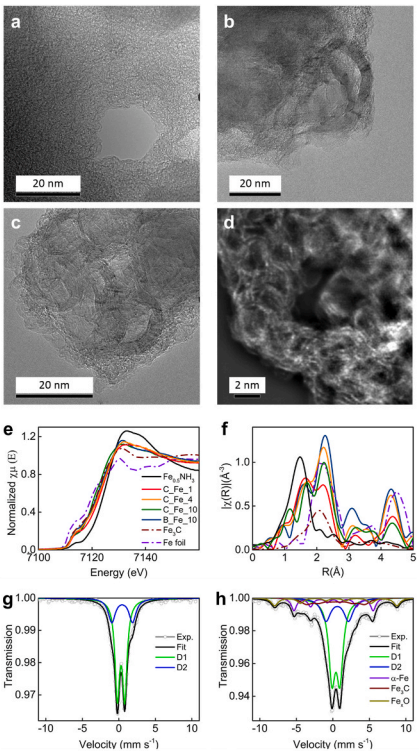

Fig. 1. Synthesis and characterization of Fe-N-C catalysts. High-resolution TEM images of (**a**) $Fe_{0.5}NH_3$, (**b**) C_Fe_1 and (**c**) C_Fe_10. (**d**) Representative STEM image of C_Fe_10. (**e**) *Ex situ* XANES spectra of catalyst powders and reference spectra of pure Fe phases (Fe foil and Fe_3C). (**f**) FT-EXAFS spectra for catalyst powders and reference pure Fe phases (Fe foil and Fe_3C), with Fe foil intensity scaled (Fe foil × 0.3). The distances in R space are uncorrected for phase shift. ^{57}Fe Mössbauer spectra measured at 5 K and fitted components for (**g**) $Fe_{0.5}NH_3$ and (**h**) C_Fe_4.

under identical conditions to C_Fe_10, but without ZIF-8. B_Fe_10 also showed reduced BET area (559 $m^2\ g^{-1}$) and a sharp (002) XRD peak (Fig. S2), suggesting that graphitization can occur via thermal treatment alone, driven by carbon matrix reorganization without external deposition. To quantitatively estimate the degree of graphitization, Raman spectra were collected for selected samples (Fig. S3). After a short CVD duration, the peak at ~2700 cm^{-1} suggests the presence of graphitic carbon structures [24–26]. However, the overall degree of graphitization of C_Fe_4 remains comparable to that of pristine $Fe_{0.5}NH_3$, suggesting that graphitized carbon constitutes only a minor fraction of the carbon matrix at this stage. In contrast, an increase in graphitization was observed after 10 h of CVD treatment for both B_Fe_10 and C_Fe_10, as indicated by the lower intensity ratio of the D band to G band (Fig. S3). These results suggest that prolonged high-temperature treatment promotes further reorganization of CNTs and that Fe-assisted graphitization plays a critical role in determining the overall graphitic character of the carbon matrix. In coated catalysts, enhanced graphitization is assigned to (i) reorganization of the pre-existing carbon matrix, and possible (ii) deposition of a graphitic N-C overlayer from ZIF-8-derived gas-phase precursors. The latter possibility is experimentally supported with online DEMS, as discussed later in Section 2.4.

XRD patterns of C_Fe_*x* and B_Fe_10 also exhibited additional diffraction peaks corresponding to metallic Fe and Fe oxide phases, which were absent in $Fe_{0.5}NH_3$. This confirms partial reduction of Fe-N_4 sites to Fe^0 nanoparticles (Fig. S2, Supplementary Note 1). These Fe particles are likely oxidized upon exposure to air, forming surface Fe oxides. The interaction between Fe species and gaseous decomposition products from ZIF-8 is discussed in more detail in Supplementary Note 1. Notably, CNTs were observed by TEM in coated samples, but not in B_Fe_10 (Fig. S4), and the Fe nanoparticles in B_Fe_10 were encapsulated by thicker carbon shells. These differences suggest that coated and uncoated catalysts undergo distinct graphitization pathways during thermal treatment.

Despite the formation of Fe nanoparticles, atomically dispersed Fe remains detectable. An aberration-corrected STEM image of C_Fe_10 directly revealed single Fe atoms (Fig. 1d), indicating that CVD-treated samples contain a mixture of Fe-N_4 sites and metallic Fe species, with shorter dwell times likely retaining more Fe-N_4 sites. XANES spectra showed a progressive decrease in white-line intensity and a redshift in edge position with increasing CVD duration, indicating a decrease in the average Fe oxidation state (Fig. 1e). FT-EXAFS spectra showed dual Fe-N (1.4 Å) and Fe-Fe (~2.2 Å, uncorrected for phase shift) coordination peaks, confirming the coexistence of Fe-N_4 sites and Fe^0 species (Fig. 1f). Linear-combination fitting (LCF) analysis of XANES data (Fig. S5 and associated discussion) indicated that Fe-N_4 site retention decreases with dwell time: 58%, 44% and 28% for C_Fe_1, C_Fe_4, and C_Fe_10, respectively. The control B_Fe_10 retained 29% of Fe-N_4 sites. Low-temperature Mössbauer spectra (5 K) of $Fe_{0.5}NH_3$ and C_Fe_4 showed both D1 and D2 Fe-N_4 site types, with C_Fe_4 also containing sextets attributed to α-Fe, Fe_3C and iron oxide (Fig. 1g and h, Table S1). The Fe-N_4 contribution in C_Fe_4 was 66%, with a D2/D1 ratio of 0.42, only slightly higher than $Fe_{0.5}NH_3$ (0.38). This suggests that CVD does not selectively convert D1 to D2 sites, contrasting with a previous report where ZIF-8 CVD increased D2/D1 from 0.44 to 0.79 [19]. Thus, ZIF-8-derived CVD treatment significantly alters the porosity, graphitization and Fe speciation in Fe-N-C catalysts. While graphitization can occur without ZIF-8, deposition of an external N-C layer is unique to the coated samples and will be further examined in the following section using online DEMS.

2.2. Catalyst activity and durability in liquid electrolyte

To explore the effect of ZIF-8-derived CVD treatment on oxygen reduction reaction (ORR) activity, we conducted rotating disk electrode (RDE) measurements in O_2-saturated 0.5 M H_2SO_4 at 25 °C. The kinetic current density (j_k) at 0.85 V_{RHE} was calculated using the Koutecky-Levich equation to correct for mass transport limitations (Fig. 2a and b). The $Fe_{0.5}NH_3$ catalyst exhibited a j_k of 3.83 mA cm^{-2}. In contrast, the CVD-coated catalysts showed progressively lower ORR activities with increasing dwell time: 1.66, 1.23 and 1.05 mA cm^{-2} for C_Fe_1, C_Fe_4 and C_Fe_10, respectively. The control sample, B_Fe_10, prepared without ZIF-8, had a j_k of 1.43 mA cm^{-2} (Fig. 2b). To understand the origin of the activity loss, j_k values were correlated with bulk Fe-N_4 site density, estimated by linear combination fitting (LCF) of Fe K-edge XANES (Fig. S5). As shown in Fig. 2b, j_k decreased with declining Fe-N_4 site density (SD_{LCF}), confirming that prolonged CVD treatment reduces active site density.

To complement this, electrochemically accessible Fe-N_4 sites were quantified using nitrite stripping voltammetry, which measures the charge associated with nitrosyl ligand reduction at Fe-N_4 sites (see Methods) [27,28]. The $Fe_{0.5}NH_3$ showed a site density (SD_{NO}) of (2.7 ± 0.1) × 10^{19} sites·g^{-1}, consistent with previous reports [29]. C_Fe_1 and C_Fe_4 retained SD_{NO} values of (2.5 ± 0.4) × 10^{19} and (2.1 ± 0.2) × 10^{19} sites·g^{-1}, respectively, while C_Fe_10 and B_Fe_10 showed significantly lower values of (1.2 ± 0.3) × 10^{19} and (1.1 ± 0.2) × 10^{19} sites·g^{-1} (Fig. S6–S7, Fig. 2c). These trends were further validated using cyanide poisoning (SD_{CN}), following a published protocol [30]. The SD_{CN} were consistent with SD_{NO} in both trend and magnitude (Fig. S8, Fig. 2d). Together, these results show that the CVD process, with or without the presence of ZIF-8 upstream, reduces both the bulk and accessible Fe-N_4 site densities, with significant reduction observed at longer dwell times.

To assess intrinsic site activity, the turnover frequency (TOF) at 0.85 V_{RHE} was calculated using both SD_{NO} and SD_{CN}, respectively (Fig. 2c and d, right y-axis). $Fe_{0.5}NH_3$ had significantly higher TOF than all CVD-treated samples. Notably, the TOF dropped sharply from $Fe_{0.5}NH_3$ to

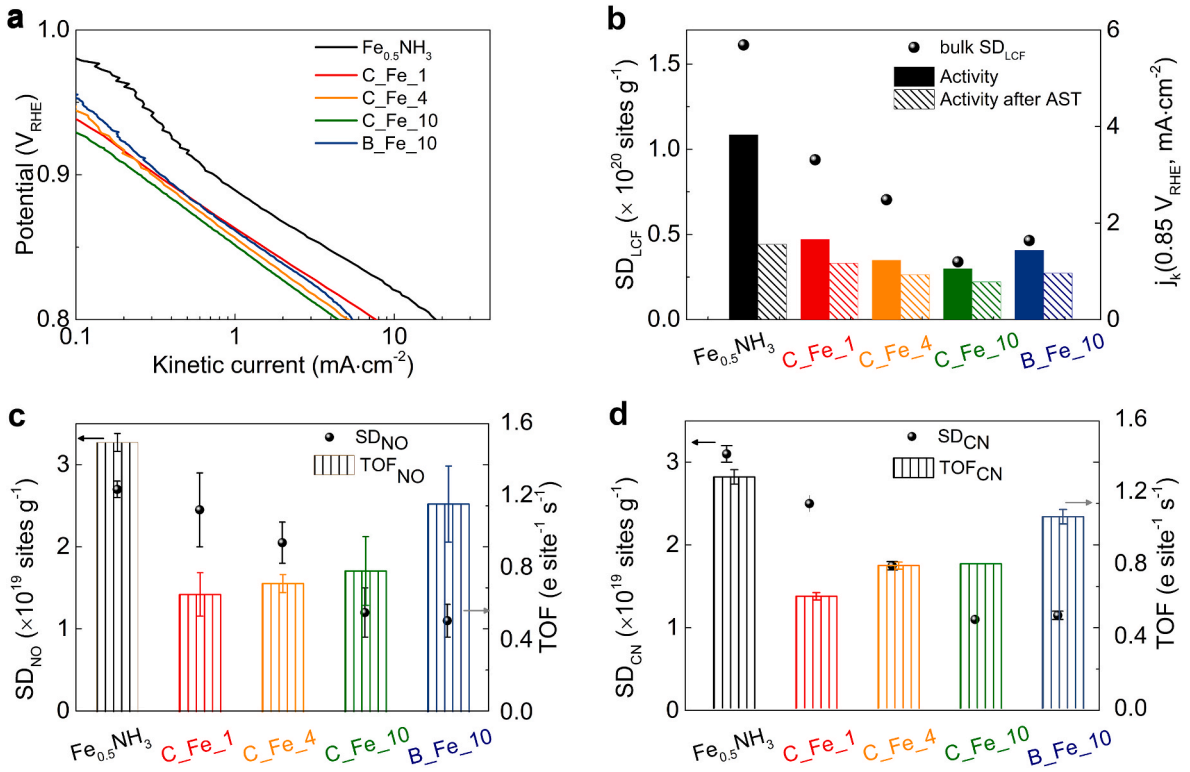

Fig. 2. Electrochemical characterization of catalysts in liquid electrolyte. (**a**) Tafel plots derived from initial ORR polarization curves in O_2-saturated 0.5 M H_2SO_4. (**b**) Fe-N_4 site density derived from LCF of XANES (circles and left y-axis) and ORR kinetic current density at 0.85 V_{RHE} before and after 1000 potential cycles (columns and right y-axis). Each cycle consists of a linear potential scan between 0.8 V_{RHE} and 1.2 V_{RHE} at 800 mV s^{-1} with a 3-s hold at each potential in O_2-saturated 0.5 M H_2SO_4 electrolyte. (**c**) Fe-N_4 site density measured by nitrite stripping and corresponding TOF values estimated at 0.85 V_{RHE}. (**d**) Fe-N_4 site density measured by cyanide poisoning and corresponding TOF values estimated at 0.85 V_{RHE}.

C_Fe_1, but varied little between C_Fe_1 and C_Fe_10, suggesting that early-stage coating substantially affects Fe-N_4 site reactivity, likely due to changes in local electronic structure or partial surface coverage. The sharp decrease in TOF observed for C_Fe_1 can be attributed to changes in the local Fe-N_4 coordination. XPS N 1s spectra (Fig. S9) show a pronounced decrease in the intensity of the ~398–399 eV component (assigned mainly to pyridinic N) relative to the intensity of the ~400–402 eV component (associated mainly with hydrogenated or protonated in-plane nitrogen groups [31]), when comparing C_Fe_1 to $Fe_{0.5}NH_3$. This is in line with the known high surface basicity of NH_3-pyrolyzed Fe-N-C catalysts but associated with their low stability in acidic media [2,32]. In contrast, the higher relative proportion of hydrogenated in-plane nitrogen groups in the coated catalysts implies lower surface basicity and a decreased Fe demetallation rate from Fe-N_4 sites in acid, which is typically associated with a lower TOF. Beyond 1 h of CVD, further structural evolution has diminishing effects on TOF. Collectively, these results indicate that the CVD process suppresses ORR activity through a dual mechanism: (i) loss of Fe-N_4 sites (lower SD) and (ii) reduced intrinsic activity per site (lower TOF). Both effects are more pronounced with longer CVD durations.

To evaluate durability, accelerated stress tests (ASTs) were conducted by cycling the potential 1000 times between 0.8 and 1.2 V_{RHE} at 800 mV·s^{-1} with a 3-s hold at each potential in O_2-saturated 0.5 M H_2SO_4. After AST, $Fe_{0.5}NH_3$ retained 1.56 mA cm^{-2} at 0.85 V_{RHE}, corresponding to ~59% activity loss (Fig. 2b). In contrast, C_Fe_1, C_Fe_4 and C_Fe_10 catalysts had 1.17, 0.93, and 0.78 mA cm^{-2}, losing only 30%, 24% and 26% activity, respectively. The control B_Fe_10 retained 0.97 mA cm^{-2} with a 33% loss (Fig. 2b). These results confirm that the ZIF-8-derived CVD process imparts greater durability, despite its adverse effect on initial ORR activity. The observed activity-durability trade-off is attributed to competing structural effects including Fe-N_4 site loss, graphitic overlayer formation, and nanoparticle generation, all modulated by the CVD duration.

2.3. ORR activity and durability in PEM fuel cells

To evaluate the effect of the CVD process on ORR activity and durability under practical operating conditions, Fe-N-C catalysts were integrated as cathode layers in membrane electrode assemblies (MEAs) and tested in H_2/O_2 PEMFCs. Each sample was evaluated by recording a beginning-of-test (BOT) polarization curve, followed by a 100-h durability hold at 0.5 V, and concluded with an end-of-test (EOT) polarization curve. At 0.80 V, where ORR kinetics dominate and mass transport limitations are minimal, $Fe_{0.5}NH_3$ delivered a BOT current density of 139 mA cm^{-2}, while C_Fe_1, C_Fe_4, C_Fe_10 yielded significantly lower values of 31, 21 and 20 mA cm^{-2}, respectively (Fig. 3a). B_Fe_10 showed 31 mA cm^{-2}, indicating that CVD treatment regardless of ZIF-8 presence decreases the BOT kinetic activity in PEMFCs, consistent with RDE measurements. At 0.50 V, where mass transport limitations become more prominent, $Fe_{0.5}NH_3$ delivered 1180 mA cm^{-2}, outperforming C_Fe_1 (539 mA cm^{-2}), C_Fe_4 (414 mA cm^{-2}), and C_Fe_10 (306 mA cm^{-2}). Notably, B_Fe_10 reached 838 mA cm^{-2}, higher than all CVD-coated samples. This suggests that the N-C overlayer formed during CVD may limit reactant access to active sites, as supported by the relative higher mesopore volume of B_Fe_10 compared with the coated samples (Fig. S2).

During the 100-h durability test at 0.5 V in H_2/O_2 PEM fuel cells, $Fe_{0.5}NH_3$ experienced continuous current decay, with a rapid loss occurring within the first 10 h (Fig. 3b). It is a typical degradation behavior of NH_3-treated Fe-N-C catalysts in PEM fuel cells [20,32]. In contrast, C_Fe_1 showed a distinct two-stage behavior with an initial increase in current density during the first 15 h (Fig. 3b inset), followed

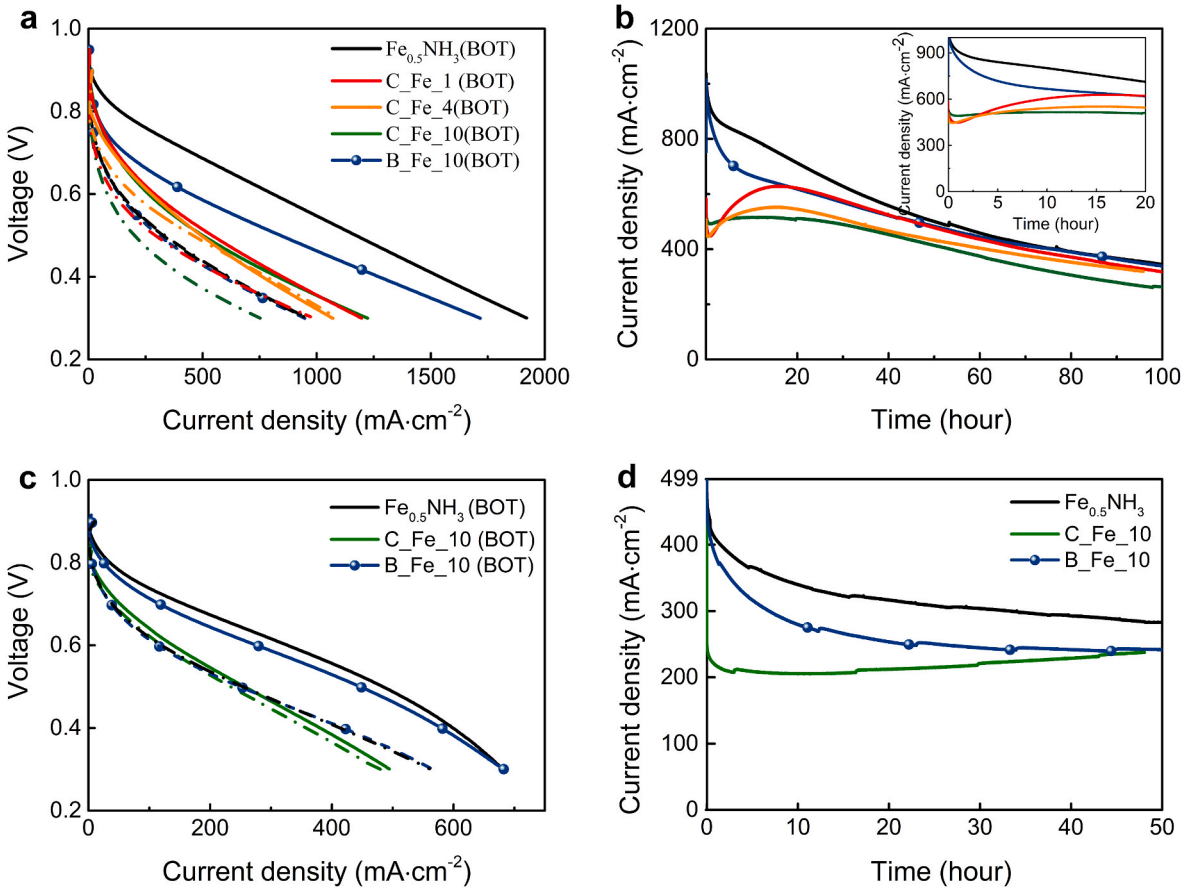

Fig. 3. Electrochemical characterization of Fe-N-C catalysts in PEMFCs. (a) Polarization curves at the beginning of test (BOT, solid curves) and end of test (dashed curves) in H_2/O_2 PEMFC. (**b**) Current density vs. time at 0.5 V cell voltage for 100 h in H_2/O_2 PEMFCs. Inset: Current density vs. time for the first 20 h in H_2/O_2 PEMFCs, as derived from (**b**). Test conditions: H_2 flow: 100 mL min^{-1}, O_2 flow: 100 mL min^{-1}, absolute pressure: 200 kPa, 80 °C, 100% RH, 4 mg cm^{-2} cathode catalyst loading. (**c**) BOT and EOT (dashed) polarization curves in H_2/air PEMFCs. (**d**) Current density vs. time at 0.5 V for 50 h in H_2/air PEMFC. Test conditions: H_2 flow: 500 mL min^{-1}, air flow: 1000 mL min^{-1}, absolute pressure: 150 kPa, 80 °C, 100% RH, 4 mg cm^{-2} cathode catalyst loading.

by a gradual decline (Fig. 3b). This activation likely results from partial removal or restructuring of the surface N-C overlayer under operating conditions, which could improve reactant accessibility to Fe-N_4 sites. A similar but less pronounced activation behavior was observed for C_Fe_4. In contrast, C_Fe_10 showed minimal activation during the first 20 h, suggesting that a more stable coating was formed with prolonged CVD treatment (Fig. 3b inset). The activation behavior is likely associated with restructuring of the surface N-C overlayer when holding the cell voltage at 0.5 V. Partial oxidation of the disordered carbon surface can generate additional porosity (without destroying sub-surface active sites), thereby improving reactant accessibility to Fe-N_4 active sites, and leading to the enhanced performance at 0.5 V during the early activation stage. Last, B_Fe_10 initially exhibited slightly higher initial current density than $Fe_{0.5}NH_3$, but underwent more rapid degradation within the first 10 h, followed by a slower decline, similar to the behavior of $Fe_{0.5}NH_3$. These results collectively demonstrate that CVD process with ZIF-8 improves stability, and ZIF-8-derived coating provides superior resistance to early degradation under PEM fuel cell conditions.

To further validate these trends, selected catalysts ($Fe_{0.5}NH_3$, C_Fe_10 and B_Fe_10) were evaluated under more realistic conditions in H_2/air PEM fuel cells. During a 50-h hold at 0.5 V, performance trends mirror those observed in H_2/O_2 tests (Fig. 3c and d). Initial ORR activity follows the order of $Fe_{0.5}NH_3$ > B_Fe_10 > C_Fe_10 (Fig. 3c). Both $Fe_{0.5}NH_3$ and B_Fe_10 experienced continuous degradation, while C_Fe_10 showed a slight increase in current density, ultimately matching the final performance of B_Fe_10 despite starting from a lower baseline (Fig. 3d). At EOT, $Fe_{0.5}NH_3$ and B_Fe_10 showed nearly overlapping polarization curves, with significant losses compared to BOT. In contrast, C_Fe_10 retained nearly identical BOT and EOT curves, demonstrating exceptional durability (Fig. 3c). However, its absolute performance remained lower than that of $Fe_{0.5}NH_3$ and B_Fe_10, reaffirming the activity-durability trade-off introduced by the CVD coating. A high durability is thus achieved for C_Fe_10, despite the significant presence of Fe particles in this catalyst. Although Fe nanoparticles formed during CVD may influence ORR durability through indirect pathways such as increased peroxide formation during ORR, the observed durability trends suggest that these effects are not dominant, at least up to 100 h operation in PEMFC. Notably, C_Fe_10 contains the highest content of Fe nanoparticles and exhibits slightly higher H_2O_2 yield than $Fe_{0.5}NH_3$ (as measured by rotating ring disk electrode, Fig. S10), yet shows superior durability. This indicates that enhanced stability of the carbon matrix plays a key role in suppressing degradation, likely outweighing potential adverse effects associated with the presence of Fe nanoparticles in CVD coated catalysts, at least in the 0–100 h timescale.

These results indicate that the ZIF-8-derived CVD coating sacrifices initial activity by lowering Fe-N_4 site density, accessibility and TOF of Fe-N_4 sites, but significantly enhances structural integrity and durability in PEMFCs. The improved stability of B_Fe_10 also suggests that high-temperature pyrolysis alone promotes beneficial carbon reorganization. However, the ZIF-8-derived overlayer offers additional protection, likely arising from N-doping or surface reconstruction. To elucidate whether these improvements result from Fe site stabilization, resistance to carbon matrix oxidation, or both, the next section presents real-time

analysis using online ICP-MS and differential electrochemical mass spectrometry (DEMS) to decouple Fe demetallation and carbon corrosion mechanisms.

2.4. Mechanistic insights into durability enhancement

Although the CVD-coated catalysts exhibited enhanced ORR durability in both RDE and PEMFC testing, the underlying degradation mechanisms required further investigation. In Fe-N-C catalysts, Fe demetallation and carbon corrosion are widely recognized as dominant degradation pathways [12,15,33,34]. To decouple these effects, we employed online inductively coupled plasma mass spectrometry (ICP-MS) and online differential electrochemical mass spectrometry (DEMS) to monitor Fe dissolution and CO_2 evolution in real time.

Fe dissolution was measured using online ICP-MS with a gas-diffusion electrode (GDE) flow cell. At room temperature, there was no significant difference in Fe leaching between $Fe_{0.5}NH_3$ and the coated catalysts. However, at 80 °C, the control sample B_Fe_10 exhibited significantly higher Fe dissolution than $Fe_{0.5}NH_3$, while C_Fe_10 exhibited a much lower rate despite having a similar Fe nanoparticle fraction (Fig. 4a, Fig. S11). Full details are provided in Supplementary Note 2. These observations suggest that in C_Fe_10, Fe nanoparticles are at least partially protected by the CVD-derived carbon coating, whereas in B_Fe_10, they remain more exposed. The difference arises from the presence of an external carbon source during CVD in C_Fe_10, which promotes the formation of graphitic carbon shells and even carbon nanotubes that encapsulated Fe nanoparticles. Such graphitic shells are known to suppress Fe dissolution [35,36]. In contrast, B_Fe_10 experiences a distinct Fe-catalyzed graphitization pathway that favors iron carbide formation rather than effective carbon encapsulation. See Supplementary note 1 and note 2 for further discussions. Nevertheless, since Fe dissolution at these conditions is dominated by Fe nanoparticles rather than by atomically dispersed Fe-N_4 sites, it is challenging to directly correlate Fe leaching with ORR degradation across all samples. To clearly reveal the lack of correlation between activity loss and Fe dissolution, the ORR activity was measured before and after the same potential cycling applied in the online ICP-MS measurements (at 25 °C), namely three scans between 0 and 1.0 V_{RHE} at 5 mV s^{-1} in Ar-saturated 0.1 M $HClO_4$. The loss in kinetic current density at 0.8 V_{RHE} follows the order of $Fe_{0.5}NH_3$ > B_Fe_10 > coated Fe-N-C catalysts (Fig. S10). However, the dissolved Fe amount measured follows a different trend: B_Fe_10 > C_Fe_10 > $Fe_{0.5}NH_3$ > C_Fe_4 > C_Fe_1 (Fig. 4a). This mismatch indicates that Fe dissolution measured by ICP-MS cannot be correlated with the stability of Fe-N_4 sites, as dissolution originates mainly from Fe particles in some catalysts (B_Fe_10), mainly from Fe-N_4 sites in others ($Fe_{0.5}NH_3$) and from both sources in the coated samples.

To further explore the protective effect of the N-doped carbon layer, we resorted to online DEMS to monitor CO_2 evolution (*m/z* 44) during cyclic voltammetry (0.0 to 1.5 V_{RHE}, 5 mV s^{-1}) at room temperature. The cumulative CO_2 signal follows the trend: $Fe_{0.5}NH_3$ > C_Fe_1 > C_Fe_4 > B_Fe_10 > C_Fe_10 (Fig. 4b and c), indicating reduced corrosion in all coated samples and B_Fe_10. Since carbon corrosion strongly depends on surface area [37], signals were normalized by BET surface area (Fig. 4d, Fig. S12f). After normalization, C_Fe_10 showed the lowest CO_2 emission, while B_Fe_10 exhibited ~37% higher CO_2 release. This confirms that ZIF-8-derived CVD coating offers more effective surface passivation than heat treatment alone. The key factor is the external carbon source introduced during CVD, which enables the deposition of graphitized carbon layers on the catalyst surface. In this case, the volatile decomposition products of ZIF-8 are the main carbon source for constructing the carbon layers. This implies that these layers can cover the pre-existing carbon surface without (or with minimal) involvement of the iron sites. The deposited layers enhance oxidation resistance and, more importantly, largely preserve the structural integrity of Fe-N_4 sites

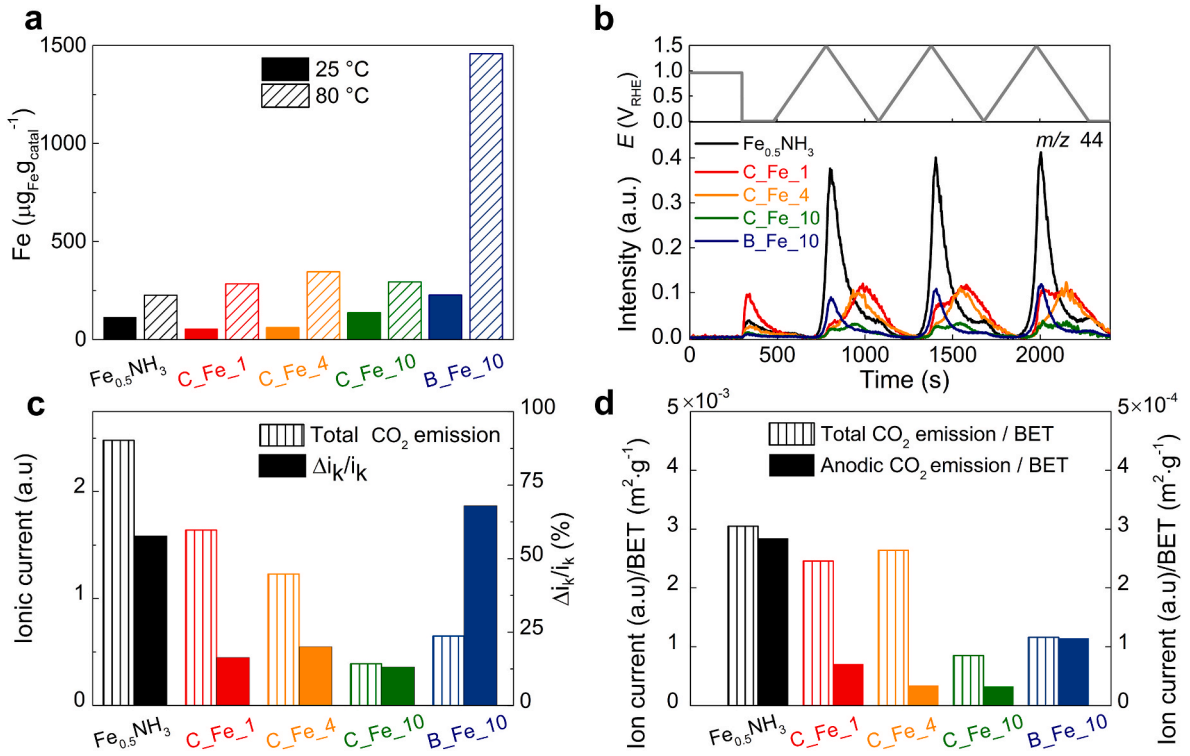

Fig. 4. Effect of CVD pyrolysis on Fe demetallation and carbon oxidation in Fe-N-C catalysts. (**a**) Total Fe dissolution accumulated during CV cycling at 5 mV s^{-1} between 0.0 and 1.0 V_{RHE} at 25 °C and 80 °C, respectively, recorded by online ICP-MS. (**b**) Online DEMS signals at *m/z* 44 (CO_2) monitored over three consecutive CVs between 0.0 and 1.5 V_{RHE}. (**c**) Total CO_2 emission amount (left y-axis) and relative ORR kinetic current (i_k) loss at 0.85 V_{RHE} (right y-axis) measured throughout the DEMS tests. (**d**) Total CO_2 emission amount normalized by BET surface area (left y-axis) and CO_2 emission amount during anodic scan from 0.0 to 1.5 V_{RHE} (value averaged over the three anodic scans) normalized by BET surface area (right y-axis).

through the formation of a local graphitic layer. In contrast, with heat treatment alone, there are no labile carbon atoms. The combination of high temperature and the presence of iron results in catalyzed graphitization, involving the diffusion of carbon atoms from the pre-existing carbon matrix. Unlike under CVD conditions, this process leads to the destruction of Fe-N_4 sites and the formation of Fe particles, which in turn catalyze the graphitization process. As a result, the induced graphitization is non-uniform in the resulting material. Graphitization occurs primarily in regions rich in Fe particles (lacking or having few Fe-N_4 sites), and no additional carbon surface layer or significant graphitization is expected in regions rich in Fe-N_4 sites. Consequently, the ability of heat treatment alone to passivate the surface and protect Fe-N_4 sites is comparatively limited.

Additionally, the potential-dependent CO_2 evolution profiles reveal distinct behaviors. In $Fe_{0.5}NH_3$ and B_Fe_10, CO_2 evolution began around 1.1 V_{RHE} in the anodic scan, peaked just after 1.5 V_{RHE} (in the cathodic scan), and then dropped sharply, followed by a plateau between 0.4 and 0.0 V_{RHE}. This late-stage CO_2 release is attributed to non-oxidative CO_2 evolution, i.e., delayed decarboxylation of oxygenated surface groups [38]. In contrast, the coated catalysts exhibited a delayed CO_2 onset (*ca.* 1.25 V_{RHE}) and a fundamentally different cathodic profile. Their CO_2 emission plateaued between 1.3 and 1.0 V_{RHE}, increased again near 0.4 V_{RHE} before declining. This behavior is consistent with previously reported non-oxidative CO_2 release from surface groups formed during high-potential cycling [39,40]. Generally, carbon corrosion in carbon blacks and other supports is dominated by anodic CO_2 peaks during CV cycling up to ~1.4 V_{RHE}, with cathodic CO_2 playing a minor role [10,38]. This pattern was observed for $Fe_{0.5}NH_3$ and B_Fe_10, but it is notably different in coated catalysts. To better quantify anodic corrosion (more relevant under typical PEMFC cathode voltages), we integrated CO_2 emission from 0 to 1.5 V_{RHE}. Notably, C_Fe_10 showed a 15 × lower anodic CO_2 emission output than $Fe_{0.5}NH_3$ (Fig. 4d–Fig. S13f), confirming the formation of a highly passivated surface resistant to oxidative degradation.

To evaluate the effect of carbon corrosion on catalytic activity, ORR activity at 0.85 V_{RHE} was measured before and after applying the same CV cycling protocol as used in the DEMS measurements (Fig. 4c, filled bars). The relative activity loss followed the order B_Fe_10 > $Fe_{0.5}NH_3$ ≫ C_Fe_4 > C_Fe_1 > C_Fe_10. Despite comparable levels of CO_2 evolution, B_Fe_10 exhibited greater ORR activity loss than any coated sample, suggesting that its enhanced graphitization occurred primarily in Fe-depleted domains, leaving Fe-N_4 sites exposed. In contrast, the coated catalysts retained significantly higher activity, indicating that the CVD-derived N-doped carbon layer suppresses oxidative degradation of the carbon matrix supporting Fe-N_4 sites, thereby preserving their structural integrity while remaining sufficiently porous to maintain reactant access. The deposited carbon must have formed a thin, but likely non-uniform and/or porous overlayer that partially passivates the carbon surface and the local environment surrounding Fe-N_4 sites, protecting the latter and their local environment from fast carbon corrosion during operation. This partial coverage (if more ordered than the carbon substrate) can reduce the total carbon oxidation and structural degradation while still allowing access (but at a slightly slower rate) of oxygen and protons to the active sites, thereby preserving ORR activity. Collectively, the ICP-MS and DEMS results clarify that carbon surface passivation is the primary mechanism behind the enhanced durability of CVD-coated Fe-N-C catalysts, as the carbon overlayer suppresses carbon corrosion and stabilizes ORR activity over time.

2.5. Thermal evolution of ZIF-8 and the parent catalyst

To investigate the volatile species produced from ZIF-8 decomposition and that are responsible for carbon coating and catalyst transformation during CVD, we monitored the thermal evolution of ZIF-8 using simultaneous thermogravimetry-mass spectrometry (TG-MS). The sample was heated from 100 to 1050 °C at 15 °C·min^{-1}, followed by a 4-h dwell at 1050 °C. An initial mass loss (~3.5 wt%) occurred between 100 and 500 °C, attributed to the decomposition of excess 2-methylimidazole ligands, as indicated by the presence of fragments at *m/z* 14, 41, 42, 44, and 54 (Fig. S14). The main decomposition occurred between 500 and 1050 °C, resulting in a loss of ~57 wt% and comprising three distinct stages (Fig. 5a and b, Fig. S15). Stage 1 (500–730 °C) has a 17 wt % loss, mainly related to the breakdown of the ZIF-8 framework, releasing H_2 (*m/z* 1, 2), low-m/z fragment ions assigned to CH_x (*m/z* 12, 14, 15, 16), and nitrogenous/C_2-fragments such as HCN^+, $C_2H_4^+$ and $C_2H_5^+$ (*m/z* 27, 28, 29) (Fig. 5b, Figs. S14 and S16). Stage 2 (730–950 °C) has a 25 wt% loss, associated with the continued emission of C- and N-containing fragments, with a gradual decline in methyl-based signals. Stage 3 (950–1050 °C) has an additional 15 wt% loss, with continued evolution of species at *m/z* 27 and *m/z* 28 (Fig. 5b, Fig. S16). The *m/z* 28 signal may arise from multiple contributors, including CO, N_2, and C_2H_x fragments, which cannot be unambiguously distinguished by MS alone. Last, during the 4-h dwell at 1050 °C, an additional 11 wt% loss occurred, leaving a final residue of ~32 wt%. This loss is related to the continuous emission of C-, N- and H- fragments (Fig. 5a, Fig. S17) and potentially high *m/z* Zn-containing fragments beyond the detection range of the instrument used in this study.

These results indicate that ZIF-8 decomposes to produce a highly reducing gas environment rich in hydrocarbons and nitrogenous species (e.g. H_2, CH_x, C_2H_x, HCN). These species play two critical roles during the CVD process: (i) partially reducing Fe-N_4 sites to form Fe nanoparticles, and (ii) serving as carbon and nitrogen precursor to deposit a N-doped carbon layer over the parent catalyst and initiate the growth of carbon nanotubes via Fe nanoparticles catalysis. Future studies using N-free carbon precursors could be useful to clarify the role of nitrogen in the deposited layer.

To mimic the pyrolysis conditions of the control sample (B_Fe_10), the parent $Fe_{0.5}NH_3$ was also monitored by TG-MS under the same thermal profile (Fig. 5c and d). 3 wt% loss occurred between 100 and 500 °C, primarily due to desorption of absorbed water, and release of carbon fragment (*m/z* 12), methyl group (*m/z* 14, 15), and C_2-containing fragments $C_2H_5^+$ (*m/z* 29), or CO_2 (*m/z* 44) (Fig. 5d, Fig. S18). An additional ~3 wt% loss between 500 and 1050 °C was associated with continued emission of hydrogenated C- and N-fragments (*m/z* 27, 28) along with continued release of carbon fragment (Fig. 5d, Fig. S18). A further 8 wt% loss during the 4-h dwell at 1050 °C was primarily attributed to continued emission of C, N- and H-containing volatile species (Fig. S19). Unlike ZIF-8, the parent $Fe_{0.5}NH_3$ released fewer volatile compounds during pyrolysis. However, it underwent substantial structural reorganization, promoting graphitization and facilitating the conversion of Fe-N_4 moieties into metallic Fe nanoparticles.

3. Conclusions

In this study, chemical vapor deposition (CVD) using ZIF-8 at 1050 °C for varying durations was conducted to coat a pre-synthesized Fe-N-C catalyst. The thermal decomposition of ZIF-8 released C-, N-, and H-containing volatile species that affected both the bulk and surface structure of the catalyst. Prolonged CVD treatment partially converted Fe-N_4 sites into Fe nanoparticles, leading to a reduced initial ORR activity. This transformation occurred irrespective of the presence of ZIF-8. However, carbon nanotube formation was observed only in the presence of ZIF-8, contributing to enhanced graphitization. With increasing CVD duration, Fe nanoparticle growth and carbon restructuring became more pronounced, resulting in larger and more ordered nanotubes and a surface with improved resistance to corrosion. Although these changes reduced the density and intrinsic activity of Fe-N_4 sites, they significantly improved the resistance to carbon oxidation and improved the overall catalyst durability in both RDE and PEMFC testing.

In summary, the ZIF-8 CVD process introduces a clear trade-off

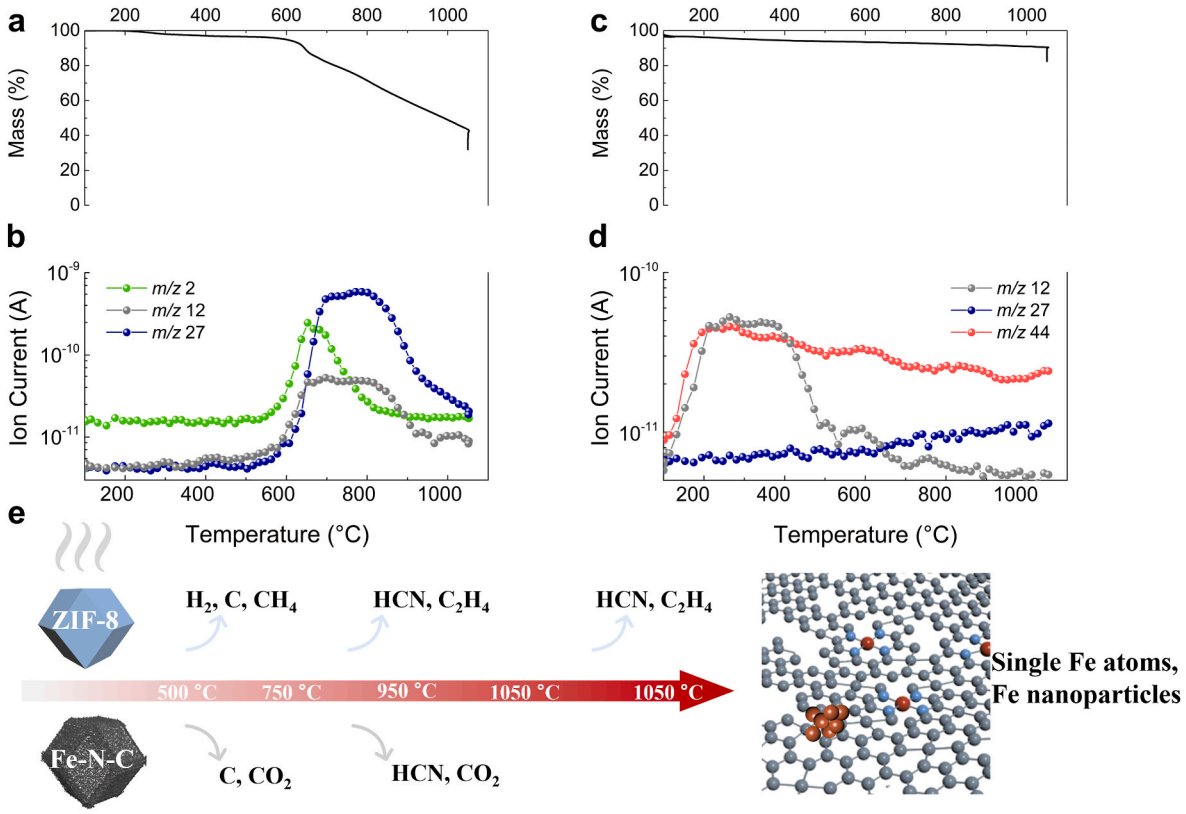

Fig. 5. Thermogravimetric analysis (TGA) and mass spectrometry (MS) of ZIF-8 and of $Fe_{0.5}NH_3$ catalyst. (**a**) TGA curve of ZIF-8. (**b**) Simultaneous MS signals of volatile fragments detected in the exhaust gases during TGA test of ZIF-8. (**c**) TGA curve of $Fe_{0.5}NH_3$. (**d**) Simultaneous MS signals of volatile fragments detected in the exhaust gases during TGA test of $Fe_{0.5}NH_3$. (**e**) The scheme of thermal decomposition products of ZIF-8 and $Fe_{0.5}NH_3$ catalyst.

between activity and durability, reducing initial performance while significantly extending catalyst lifetime. These findings provide mechanistic insights into the degradation of Fe-N-C catalysts and identify carbon surface passivation as a promising strategy for developing durable, high-performance PGM-free catalysts for fuel cell applications.

4. Experimental methods

4.1. $Fe_{0.5}NH_3$ synthesis

The $Fe_{0.5}NH_3$ catalyst was synthesized as previously described in our reports [2]. In this work, ZIF-8 nanocrystals (80 nm) were synthesized following our previously reported method [8], replacing the commercial ZIF-8 (Basolite Z1200) in the synthesis of $Fe_{0.5}NH_3$ catalyst. ZIF-8 nanocrystals (0.8 g), iron (II) acetate (15.6 mg, 0.5 wt% Fe in precursors, Sigma-Aldrich), and 1,10-phenanthroline (0.2 g, Sigma-Aldrich) were ball milled together in a zirconium oxide crucible (45 mL) containing 100 zirconium oxide balls (5 mm diameter) for 2 h at 400 rpm. The resulting powders were pyrolyzed under argon flow by heating them from room temperature to 1050 °C at a ramp rate of 5 °C min^{-1}, held at 1050 °C for 1 h under Ar flow, and then cooled to room temperature in argon. This powder, labeled as $Fe_{0.5}Ar$, was then flash-pyrolyzed at 950 °C for 5 min under NH_3 flow, yielding the $Fe_{0.5}NH_3$ catalyst. Flash pyrolysis involved pre-heating for 2 h the oven to 950 °C and flowing NH_3 shortly before the flash pyrolysis, then rapidly introducing the sample in the oven and leaving it for 5 min only. Afterward, the split hinge oven was opened and the quartz tube rapidly withdrawn to enable fast cooling, while the NH_3 flow was replaced by Ar.

4.2. Coated Fe-N-C catalyst synthesis

240 mg of ZIF-8 nanocrystals were placed in a quartz ceramic boat positioned upstream in an Ar flow (50 mL min^{-1}), and 40 mg of $Fe_{0.5}NH_3$ catalyst powder was evenly spread in a thin layer (8 × 1 cm^2) downstream in the same quartz boat, with a 1 cm distance between the ZIF-8 nanocrystals and the $Fe_{0.5}NH_3$ powder. The quartz tube was then installed in the split hinge oven and the tube was purged with Ar flow for 30 min before heating. The furnace temperature was then ramped to 1050 °C at 15 °C min^{-1} and dwelled at 1050 °C for various hours (1, 4, 10 h). After this, the tube inside of oven was allowed to cool naturally to room temperature under the same Ar flow, yielding the coated catalysts labeled as C_Fe_x, where x represents the dwell duration in hours. The control sample was prepared in the same condition as C_Fe_10 but without adding ZIF-8 nanocrystals upstream, and labeled as B_Fe_10.

4.3. Electrochemical characterization

4.3.1. RDE characterisation

Catalyst inks were prepared by dispersing 10 mg of catalyst powder in a mixture of 360 μL Millipore water and 180 μL ethanol, followed by the addition of 120 μL of 5 wt% Nafion solution (Ion Power). The mixture was sonicated for 60 min in an ice bath to maintain a temperature below 20 °C. An aliquot of the ink was drop-cast onto a glassy carbon (GC) electrode (0.1963 cm^2, Pine Instrument) to reach a catalyst loading of 800 μg cm^{-2}. The GC electrode with the deposited catalyst layer was used as the working electrode, mounted on a rotator (Pine Instruments), and connected to a potentiostat (Biologic SP300). A graphite rod and a commercial hydrogen reference electrode (Hydro-Flex, Gaskatel) were used as counter and reference electrodes, respectively. Initial oxygen reduction reaction polarization curves were collected using linear sweep voltammetry at 2 mV s^{-1} from 0.95 V to

0.05 V versus reversible hydrogen electrode (RHE) under 900 rpm in O_2-saturated 0.5 M sulfuric acid solution at room temperature. The working electrode was then subject to potential cycling in O_2-saturated 0.5 M sulfuric acid between 0.8 V_{RHE} to 1.2 V_{RHE} for 1000 cycles, with a scan rate of 800 mV s^{-1}, holding at 0.8 V_{RHE} and 1.2 V_{RHE} for 3 s each. After cycling, the end of test ORR polarization curves were recollected under the same parameters. Cyclic voltammetry (CV) curves were also collected after each ORR polarization curve in Ar-saturated 0.5 M sulfuric acid, using a scan rate of 10 mV s^{-1} with the same potential ranges.

4.3.2. Nitrite stripping

A 0.1963 cm^2 glassy carbon electrode with 200 μg cm^{-2} catalyst was used as the working electrode, while a graphite rod counter electrode and a Ag/AgCl reference electrode (RE-T1A, EC Frontier) were used in a standard three-electrode electrochemical cell. A 0.5 M acetate buffer (pH 5.2) was prepared using sodium acetate (99%, Sigma-Aldrich) and potassium hydroxide (≥99.95%, Sigma-Aldrich, trace metal basis). The experimental procedures, including cleaning, measurement, poisoning, and recovery, followed the previous report by Malko et al. [27,28] Briefly, the procedure included the following steps: (1) Cleaning the working electrode: the working electrode was subjected to potential cycling between 1.05 V to −0.4 V_{RHE} at 100 mV s^{-1} and 10 mV s^{-1} in an Ar-saturated electrolyte for 20 cycles. This process was repeated until steady-state CV data were obtained. (2) Baseline CVs were recorded between 0.4 V_{RHE} and −0.3 V_{RHE} at a scan rate of 10 mV s^{-1}. (3) Poisoning procedure: The working electrode was immersed in 0.125 M $NaNO_2$ solution (≥97.0%, Sigma-Aldrich, ACS reagent) at 300 rpm for 5 min at open-circuit potential (OCP). The electrode was then washed with deionized water (1 min), electrolyte (5 min), and deionized water (1 min) at 300 rpm. (4) Post-poisoning measurements: nitrite stripping CV were recorded in sequence. The nitrite stripping charge was integrated from CV profiles. The number of electrons transferred during nitrite stripping was determined following a previously reported protocol [41]. The active site density (SD) was then calculated based on established methods [8]. In addition, the initial ORR polarization curves were recorded for each catalyst in oxygen-saturated 0.1 M $HClO_4$ and the kinetic current density was extracted at 0.85 V_{RHE}. Finally, the TOF at 0.85 V_{RHE} was calculated by correlating the site density value with the kinetic current density.

4.3.3. In situ cyanide poisoning

The measurement protocol was adapted from a previous report [30]. A double-compartment electrochemical H-cell was used, separated by a DuPont Nafion 115 membrane, with both chambers filled with 0.1 M $HClO_4$ electrolyte. The Ag/AgCl reference electrode (RE-T1A, EC Frontier) and the graphite rod counter electrode were placed in the same chamber, while the graphite rod working electrode was mounted in the opposite chamber. The *in situ* cyanide poisoning protocol comprises four main steps. (1) Catalyst dispersion: catalyst powder (30 mg) was dispersed in the Ar-saturated electrolyte in the chamber containing the working electrode, under continuous stirring at approximately 300 rpm. The working electrode was held at OCP for 30 min under continuous Ar purging to remove dissolved O_2 from the electrolyte. (2) Oxygen removal: the working electrode was held at 0.5 V_{RHE} for approximately 20 min to remove pre-absorbed O_2 from catalysts. (3) Cyanide poisoning: the working electrode was held at 1.0 V_{RHE} for 10 min, after which 200 μM KCN was added to the electrolyte in both chambers. The cyanide concentration in working electrode chamber was measured by spectrophotometric titration. The color change of solution was monitored at 520 nm using an UV-vis spectrophotometer (Genesis 400, Thermo-Fisher Scientific) with reference to a blank electrolyte. The decrease in cyanide concentration, attributed to adsorption by the catalyst, was quantified and associated with cyanide-poisoned FeN_xC_y sites. (4) Post-poisoning analysis: the poisoned catalyst was collected from the chamber, washed by filtration. The ORR activities of both the pristine catalyst and poisoned catalyst were measured using RDE. The decay in ORR activity (at 0.85 V_{RHE}) is correlated with the cyanide-poisoned FeN_xC_y sites to estimate the SD and TOF of catalysts, as described in the previous report [30].

4.3.4. MEA preparation for PEMFC measurements

The catalysts were used to prepare cathode electrodes of MEAs tested in PEMFCs under H_2/O_2 and H_2/air conditions. The cathode catalyst inks were prepared by dispersing a calculated amount of catalyst powder and Nafion D521 dispersion (5 wt%, Ion Power) (I/C = 1.4 was used in preparing cathodes for testing in H_2/O_2, and I/C = 0.9 was used in preparing cathodes for testing in H_2/air) into DI water/1-propanol (4/1 vol ratio) aqueous solution, followed by 1 h of sonication in an ice bath. The resulting inks were drop-cast on an SGL 28-BC gas diffusion layer (Sigracet), yielding a catalyst loading of 4 mg cm^{-2}. Commercial platinum gas diffusion electrodes (0.4 $mg_{pt}cm^{-2}$ on SGL 22-BB, Fuel Cell Store) were used as anodes. The anode electrode, Nafion 211 membrane, and cathode electrode were sandwiched together and hot-pressed at 135 °C for 2 min. Each MEA was placed in a single cell with single-serpentine flow channels and tested using a fuel cell test station (Scribner 850e, Scribner Associates). The cells were conditioned in nitrogen at 100% relative humidity (RH) and 80 °C for 20 min.

4.3.5. H_2/O_2 PEMFC experiments

The CV curves between 0.0 V and 1.0 V at a scan rate of 20 mV $\cdot s^{-1}$ were collected with H_2 flow on the anode side and N_2 flow on the cathode side. Subsequently, the oxygen (flowing at 100 mL min^{-1}) and H_2 (flowing at 100 mL min^{-1}) were used as the cathode and anode reactants, respectively. The total pressure applied to the MEA was 200 KPa absolute. Oxygen reduction polarization curves were recorded from 0.95 V to 0.3 V at a scan rate of 1 mV s^{-1}, and noted as beginning-of-test (BOT) ORR activities. The cell voltage was then held at 0.5 V under the same H_2/O_2 flow rates and absolute pressures, at 100% RH and 80 °C for 100 h. End-of-test (EOT) ORR polarization curves were collected again under the same conditions as well as CV curves in H_2/N_2.

4.3.6. H_2/air PEMFC experiments

The CV curves were recorded between 0.0 V and 1.0 V at a scan rate of 20 mV s^{-1} with H_2 flow on the anode side and N_2 flow on the cathode side. Subsequently, air (1000 mL min^{-1}) and H_2 (500 mL$\cdot min^{-1}$) were used as cathode and anode reactants, respectively. The total pressure was 150 KPa absolute. Oxygen reduction polarization curves were recorded from 0.95 V to 0.3 V at 1 mV s^{-1}, noted as the BOT ORR performance. Afterward, the cell voltage was held at 0.5 V at the same H_2/air flow rates and absolute pressures at 100% RH and 80 °C for 50 h. EOT ORR polarization curves were collected under the same conditions as well as CV curves in H_2/N_2.

4.3.7. Online ICP-MS

GDEs with Fe-N-C catalysts were prepared following the previous protocols, mounted on an EFC coupled to ICP-MS. Further details were provided in the previous report [11]. The GDE was fabricated by spraying catalyst ink onto a mesoporous layer (MPL) deposited on carbon paper. The resulting MPL had a Ketjen Black EC-300J loading of 2 mg cm^{-2}. Thereafter, catalyst ink (25 mg catalyst + 10 mL isopropanol + 250 μL 5 wt% Nafion solution) was sprayed onto the MPL to reach target catalyst loadings of 400 μg cm^{-2}. The active catalyst area of the GDE was 0.096 cm^2. Fe dissolution was monitored using ICP-MS (iCAP RQ, Thermo-Fisher Science) coupled with a GDE-based EFC. The EFC is equipped with a U-shaped channel with a diameter of 1 mm and an opening for contact with the GDE. A graphite tube counter electrode was placed at the inlet, and an Ag/AgCl reference electrode was connected to the outlet of EFC. A 0.1 M $HClO_4$ electrolyte, de-aerated using a degasser (AG-32-01, FLOM Corp.), was flowed into the EFC at a flow rate of 200 μL min^{-1}. The electrolyte was mixed with 0.2 M HNO_3 containing 5 ppb ^{187}Re as an internal standard using a Y-connector (mixing ratio 1:1). Fe dissolution was tracked by subjecting working electrodes to potential

cycling between 1.0 and 0.0 V_{RHE} at 200 mV s^{-1} for 300 cycles, and subsequently at 5 mV s^{-1} for 3 cycles, in Ar-saturated 0.1 M $HClO_4$ at 25 and 80 °C, respectively.

4.3.8. Online DEMS

The setup is comprised of EFC connected to a mass spectrometer (Max 300 LG, Extrel) and more details have been previously reported [40]. The EFC was fitted with a U-shaped channel with a 10 mm diameter at the bottom to allow electrical contact with the 3 mm GC working electrode (A-011169, Bio-Logic). To collect volatile and gaseous products, a porous polytetrafluoroethylene membrane (WP-010-80, Sumitomo Electric Ind., Ltd.) was positioned approximately 100 μm above the working electrode. The graphite and Ag/AgCl reference electrodes were electrically connected to the outlet of the EFC. The catalyst loading on the working electrode was 1.0 mg cm^{-2}. The electrolyte used was Ar-saturated 0.1 M $HClO_4$, flowing at 70 μL min^{-1}. DEMS signals were collected when the working electrodes were held at OCP and 0 V_{RHE} and subsequently underwent potential scanning from 0 to 1.5 V_{RHE} at 5 mV s^{-1} for 3 cycles. Ion currents from CO_2 at *m/z* 44 were analyzed.

4.3.9. Physical characterization

4.3.9.1. XRD. X-ray diffraction patterns of catalyst powders were collected using a PANanalytical X'Pert Pro powder X-ray diffractometer with Cu Kα radiation.

4.3.9.2. N_2 adsorption-desorption analysis. The textural properties of catalyst powders, including specific surface area, pore size distribution (PSD), and pore volume, were characterized by determining nitrogen adsorption-desorption isotherms at 77 K using the 3Flex instrument (Micromeritics), equipped with three "Micropore" analysis ports including a 0.1 torr transducer with a measurement accuracy of 0.15%. Prior to N_2 sorption, the samples were first evacuated under vacuum at room temperature for 1 h, then further evacuated at 200 °C for 12 h until a stable pressure of at least 0.001 torr was reached. After the analysis, the free volume was measured with helium to prevent gas trapping in very small micropores.

The sorption isotherms were measured with nitrogen. In the low relative pressure range associated with micropore characterization, the nitrogen dose, equilibration time, and measurement step in P/P_0 were 20 cm^3 g^{-1}, 30 s, and 0.005, respectively. The PSDs of catalysts were calculated using the SAIEUS program (version 3.0) developed by Micromeritics. The standard slit-pore model (Carbon-N_2-77, NLDFT, Standard Slit) was selected and pores with diameters smaller that 5 Å were not considered due to limitation imposed by the size of the probe molecule (3.6 Å).

4.3.9.3. TEM and STEM. TEM images of Fe-N-C catalysts were recorded with a JEOL 2010 field emission gun at 200 kV. The resolution of TEM images was 0.19 nm and were performed using a 200 kV JEOL 2100F microscope equipped with a retractable large-angle Centurio Silicon Drift detector.

4.3.9.4. XAS. Fe K-edge X-ray absorption spectra were collected at SAMBA beamline (Synchrotron SOLEIL). Fe-N-C catalyst powders were pelletized as discs of 10 mm diameter with a thickness of 1 mm, using graphite powder as a binder and XAS was measured in transmission mode. The XAS data were processed using the Ifeffit−based Athena program [42].

4.3.9.5. Mössbauer spectroscopy. The ^{57}Fe Mössbauer spectrometer was operated in transmission mode with a ^{57}Co: Rh source. The velocity driver was operated in constant acceleration mode with a triangular velocity waveform. The velocity scale was calibrated with the magnetically split sextet of a high-purity α-Fe foil at room temperature. The spectra were fitted to appropriate combinations of Lorentzian profiles representing quadrupole doublets, and sextets by least-squares methods. Isomer-shift values are reported relative to α-Fe at room temperature. The fittings were performed with unconstrained parameters (relative area, isomer shift, QS, linewidth (LW), hyperfine field (H)) for each spectral component. ^{57}Fe-N-C catalysts were prepared as the other catalysts but with ^{57}Fe acetate as Fe precursor, and were mounted in a 2 cm^2 holder of Mössbauer spectrometer.

4.3.9.6. TGA-MS. The pyrolysis of ZIF-8 nanocrystals and $Fe_{0.5}NH_3$ were monitored by using TGA coupled with differential thermal analysis (DTA) on a thermogravimeter (Netzsch, STA449F1 Jupiter). The effluent gases from the TGA-DTA were analyzed using a quadrupole mass spectrometer (QMS 403 Aeolos Quadro). ZIF-8 nanocrystals and $Fe_{0.5}NH_3$ were isothermally held at 100 °C for 30 min, then ramped to 1050 °C at 15 °C min^{-1}, followed by dwelling at 1050 °C for 4 h. The tests were conducted under a steady argon flow (50 mL min^{-1}).

CRediT authorship contribution statement

Li Jiao: Writing – review & editing, Writing – original draft, Methodology, Formal analysis. **Geunsu Bae:** Methodology. **Nicolas Donzel:** Methodology. **Marc Dupont:** Resources. **Frédéric Lecoeur:** Resources. **Min Wook Noh:** Methodology. **Anastassiya Khan:** Methodology. **Andrea Zitolo:** Resources, Methodology. **Laetitia Dubau:** Methodology. **Goran Dražić:** Methodology. **Chang Hyuck Choi:** Methodology. **Frédéric Jaouen:** Writing – review & editing, Supervision, Funding acquisition.

Declaration of competing interest

The authors declare that they have no known competing financial interests or personal relationships that could have appeared to influence the work reported in this paper.

Acknowledgments

We acknowledge financial support from the French National Research Agency through the DEEP project (grant number ANR-21-CE05-0021) and the Synchrotron SOLEIL (Gif-sur Yvette, France) for provision of synchrotron radiation facilities at the SAMBA beamline. Moulay Tahar Sougrati is acknowledged for his help with the ^{57}Fe Mössbauer characterization and analyses. C.H.C acknowledges financial support from National Research Foundation of Korea grants funded by the Korea government (grant nos. RS-2022-NR068298 and RS-2024-00406517).

Appendix A. Supplementary data

Supplementary data to this article can be found online at https://doi.org/10.1016/j.jpowsour.2026.239758.

Data availability

Data will be made available on request.

References

[1] M.K. Debe, Electrocatalyst approaches and challenges for automotive fuel cells, Nature 486 (7401) (2012) 43–51.
[2] A. Zitolo, V. Goellner, V. Armel, M.T. Sougrati, T. Mineva, L. Stievano, E. Fonda, F. Jaouen, Identification of catalytic sites for oxygen reduction in iron- and nitrogen-doped graphene materials, Nat. Mater. 14 (9) (2015) 937–942.
[3] Q. Jia, N. Ramaswamy, H. Hafiz, U. Tylus, K. Strickland, G. Wu, B. Barbiellini, A. Bansil, E.F. Holby, P. Zelenay, S. Mukerjee, Experimental observation of redox-induced Fe-N switching behavior as a determinant role for oxygen reduction activity, ACS Nano 9 (12) (2015) 12496–12505.

[4] J. Li, L. Jiao, E. Wegener, L.L. Richard, E. Liu, A. Zitolo, M.T. Sougrati, S. Mukerjee, Z. Zhao, Y. Huang, F. Yang, S. Zhong, H. Xu, A.J. Kropf, F. Jaouen, D.J. Myers, Q. Jia, Evolution pathway from iron compounds to Fe1(II)-N4 sites through gas-phase iron during pyrolysis, J. Am. Chem. Soc. 142 (3) (2020) 1417–1423.
[5] E.P. Michel Lefèvre, Frédéric Jaouen, Jean-Pol dodelet iron-based catalysts with improved oxygen reduction activity in polymer electrolyte fuel cells, Science 324 (2009) 71.
[6] T. Hoon, D.A.C. Chung, Drew Higgins, Brian T. Sneed, Edward F. Holby, Karren L. More, Piotr Zelenay direct atomic-level insight into the active sites ofa high-performance PGM-free ORR catalyst, Science 357 (2017) 479.
[7] A. Mehmood, M. Gong, F. Jaouen, A. Roy, A. Zitolo, A. Khan, M.-T. Sougrati, M. Primbs, A.M. Bonastre, D. Fongalland, G. Drazic, P. Strasser, A. Kucernak, High loading of single atomic iron sites in Fe–NC oxygen reduction catalysts for proton exchange membrane fuel cells, Nat. Catal. 5 (4) (2022) 311–323.
[8] L. Jiao, J. Li, L.L. Richard, Q. Sun, T. Stracensky, E. Liu, M.T. Sougrati, Z. Zhao, F. Yang, S. Zhong, H. Xu, S. Mukerjee, Y. Huang, D.A. Cullen, J.H. Park, M. Ferrandon, D.J. Myers, F. Jaouen, Q. Jia, Chemical vapour deposition of Fe-N-C oxygen reduction catalysts with full utilization of dense Fe-N4 sites, Nat. Mater. 20 (10) (2021) 1385–1391.
[9] K. Kumar, L. Dubau, F. Jaouen, F. Maillard, Review on the degradation mechanisms of Metal-N-C catalysts for the oxygen reduction reaction in acid electrolyte: current understanding and mitigation approaches, Chem. Rev. 123 (15) (2023) 9265–9326.
[10] C.H. Choi, C. Baldizzone, J.P. Grote, A.K. Schuppert, F. Jaouen, K.J. Mayrhofer, Stability of Fe-N-C catalysts in acidic medium studied by operando spectroscopy, Angew Chem. Int. Ed. Engl. 54 (43) (2015) 12753–12757.
[11] G. Bae, M.M. Kim, M.H. Han, J. Cho, D.H. Kim, M.-T. Sougrati, J. Kim, K.-S. Lee, S. H. Joo, W.A. Goddard, H.-S. Oh, H. Kim, F. Jaouen, C.H. Choi, Unravelling the complex causality behind Fe–N–C degradation in fuel cells, Nat. Catal. 6 (12) (2023) 1140–1150.
[12] A. Pedersen, K. Kumar, Y.P. Ku, V. Martin, L. Dubau, K.T. Santos, J. Barrio, V. A. Saveleva, P. Glatzel, V.K. Paidi, X. Li, A. Hutzler, M.M. Titirici, A. Bonnefont, S. Cherevko, I.E.L. Stephens, F. Maillard, Operando Fe dissolution in Fe-N-C electrocatalysts during acidic oxygen reduction: impact of local pH change, Energy Environ. Sci. 17 (17) (2024) 6323–6337.
[13] J. Müller-Hülstede, H. Schmies, D. Schonvogel, Q. Meyer, Y. Nie, C. Zhao, P. Wagner, M. Wark, What determines the stability of Fe-N-C catalysts in HT-PEMFCs? Int. J. Hydrogen Energy 50 (2024) 921–930.
[14] K. Kumar, L. Dubau, M. Mermoux, J. Li, A. Zitolo, J. Nelayah, F. Jaouen, F. Maillard, On the influence of oxygen on the degradation of Fe-N-C catalysts, Angew Chem. Int. Ed. Engl. 59 (8) (2020) 3235–3243.
[15] U.I.K. Regis Chenitz, Michel Lefevre, Vassili Glibin, Gaixia Zhang, Shuhui Sun, Jean-Pol Dodelet A specific demetalation of Fe–N4 catalytic sites in the micropores of NC_Ar + NH3 is at the origin of the initial activity loss of the highly active Fe/N/C catalyst used for the reduction of oxygen in PEM fuel cells, Energy Environ. Sci. 11 (2018) 365–382.
[16] J. Li, S. Ghoshal, W. Liang, M.-T. Sougrati, F. Jaouen, B. Halevi, S. McKinney, G. McCool, C. Ma, X. Yuan, Z.-F. Ma, S. Mukerjee, Q. Jia, Structural and mechanistic basis for the high activity of Fe–N–C catalysts toward oxygen reduction, Energy Environ. Sci. 9 (7) (2016) 2418–2432.
[17] M.T. Sougrati, V. Goellner, A.K. Schuppert, L. Stievano, F. Jaouen, Probing active sites in iron-based catalysts for oxygen electro-reduction: a temperature-dependent 57 Fe Mössbauer spectroscopy study, Catal. Today 262 (2016) 110–120.
[18] T. Mineva, I. Matanovic, P. Atanassov, M.-T. Sougrati, L. Stievano, M. Clémancey, A. Kochem, J.-M. Latour, F. Jaouen, Understanding active sites in pyrolyzed fe–n–c catalysts for fuel cell cathodes by bridging density functional theory calculations and 57Fe Mössbauer spectroscopy, ACS Catal. 9 (10) (2019) 9359–9371.
[19] S. Liu, C. Li, M.J. Zachman, Y. Zeng, H. Yu, B. Li, M. Wang, J. Braaten, J. Liu, H. M. Meyer, M. Lucero, A.J. Kropf, E.E. Alp, Q. Gong, Q. Shi, Z. Feng, H. Xu, G. Wang, D.J. Myers, J. Xie, D.A. Cullen, S. Litster, G. Wu, Atomically dispersed iron sites with a nitrogen–carbon coating as highly active and durable oxygen reduction catalysts for fuel cells, Nat. Energy 7 (7) (2022) 652–663.
[20] E. Proietti, F. Jaouen, M. Lefevre, N. Larouche, J. Tian, J. Herranz, J.P. Dodelet, Iron-based cathode catalyst with enhanced power density in polymer electrolyte membrane fuel cells, Nat. Commun. 2 (2011) 416.
[21] Y. Zeng, C. Li, B. Li, J. Liang, M.J. Zachman, D.A. Cullen, R.P. Hermann, E.E. Alp, B. Lavina, S. Karakalos, M. Lucero, B. Zhang, M. Wang, Z. Feng, G. Wang, J. Xie, D. J. Myers, J.-P. Dodelet, G. Wu, Tuning the thermal activation atmosphere breaks the activity–stability trade-off of Fe–N–C oxygen reduction fuel cell catalysts, Nat. Catal. 6 (12) (2023) 1215–1227.
[22] D. Xia, X. Tang, S. Dai, R. Ge, A. Rykov, J. Wang, T.H. Huang, K.W. Wang, Y. Wei, K. Zhang, J. Li, L. Gan, F. Kang, Ultrastable Fe-N-C fuel cell electrocatalysts by eliminating non-coordinating nitrogen and regulating coordination structures at high temperatures, Adv. Mater. 35 (5) (2023) e2204474.
[23] L. Yang, N. Larouche, R. Chenitz, G. Zhang, M. Lefèvre, J.-P. Dodelet, Activity, performance, and durability for the reduction of oxygen in PEM fuel cells, of Fe/N/C electrocatalysts obtained from the pyrolysis of metal-organic-framework and iron porphyrin precursors, Electrochim. Acta 159 (2015) 184–197.
[24] H. Ko, Y. Pikus, C. Jiang, A. Jauss, O. Hollricher, V.V. Tsukruk, High-resolution Raman microscopy of curled carbon nanotubes, Appl. Phys. Lett. 85 (13) (2004) 2598–2600.
[25] O. Frank, L. Kavan, M. Kalbac, Carbon isotope labelling in graphene research, Nanoscale 6 (12) (2014) 6363–6370.
[26] Zheling Li, Libo Deng, Ian A. Kinloch, R.J. Young, Raman spectroscopy of carbon materials and their composites: Graphene, nanotubes and fibres, Prog. Mater. Sci. 135 (2023) 101089.
[27] D. Malko, A. Kucernak, T. Lopes, In situ electrochemical quantification of active sites in Fe-N/C non-precious metal catalysts, Nat. Commun. 7 (2016) 13285.
[28] D. Malko, A. Kucernak, T. Lopes, Performance of Fe-N/C oxygen reduction electrocatalysts toward NO(2)(-), NO, and NH(2)OH electroreduction: from fundamental insights into the active Center to a new method for environmental nitrite destruction, J. Am. Chem. Soc. 138 (49) (2016) 16056–16068.
[29] M. Primbs, Y. Sun, A. Roy, D. Malko, A. Mehmood, M.-T. Sougrati, P.-Y. Blanchard, G. Granozzi, T. Kosmala, G. Daniel, P. Atanassov, J. Sharman, C. Durante, A. Kucernak, D. Jones, F. Jaouen, P. Strasser, Establishing reactivity descriptors for platinum group metal (PGM)-free Fe–N–C catalysts for PEM fuel cells, Energy Environ. Sci. 13 (8) (2020) 2480–2500.
[30] G. Bae, H. Kim, H. Choi, P. Jeong, D.H. Kim, H.C. Kwon, K.S. Lee, M. Choi, H.S. Oh, F. Jaouen, C.H. Choi, Quantification of active site density and turnover frequency: from single-atom metal to nanoparticle electrocatalysts, JACS Au 1 (5) (2021) 586–597.
[31] K. Artyushkova, Misconceptions in interpretation of nitrogen chemistry from x-ray photoelectron spectra, J. Vac. Sci. Technol. A 38 (3) (2020).
[32] X. Yang, W. Sun, J. Chen, Y. Gao, R. Zhang, Q. Luo, T. Lyu, L. Du, The degradation of cathodic Fe/N/C catalyst in PEMFCs: the evolution of remanent active sites after demetallation, J. Mater. Sci. Technol. 173 (2024) 100–106.
[33] J. Li, M.T. Sougrati, A. Zitolo, J.M. Ablett, I.C. Oğuz, T. Mineva, I. Matanovic, P. Atanassov, Y. Huang, I. Zenyuk, A. Di Cicco, K. Kumar, L. Dubau, F. Maillard, G. Dražić, F. Jaouen, Identification of durable and non-durable FeNx sites in Fe–N–C materials for proton exchange membrane fuel cells, Nat. Catal. 4 (1) (2020) 10–19.
[34] Y. Chu, Y. Cheng, P. Wang, J. Bai, X. Guan, S. Wang, C. Lan, H. Wu, Z. Shi, S. Zhu, W. Liu, C. Liu, M. Xiao, W. Xing, Unraveling the potential-dependent degradation mechanism in Fe-N-C catalysts for oxygen reduction reaction, Sci. China Chem. 68 (4) (2024) 1541–1549.
[35] Mariko Kadowaki, Izumi Muto, Kinari Takahashi, Takashi Doi, Hiroyuki Masuda, Hideki Katayama, Kaori Kawano, Sugawara Yu, N. Hara, Anodic polarization characteristics and electrochemical properties of Fe3C in chloride solutions, J. Electrochem. Soc. 166 (2019) C345.
[36] Elli Leppänen, Sami Sainio, Hua Jiang, Bjørn Mikladal, Ilkka Varjos, T. Laurila, Effect of electrochemical oxidation on physicochemical properties of Fe-Containing single-walled carbon nanotubes, Chemelectrochem 7 (2020) 4136–4143.
[37] J. Sean, M.A. Ashton, Comparative DEMS study on the electrochemical oxidation of carbon blacks, J. Power Sources 217 (2012).
[38] J. Ashton Sean, M. Arenz, A DEMS study on the electrochemical oxidation of a high surface area carbon black, Electrochem. Commun. 13 (2011) 1473–1475.
[39] Maillard Frédéric, Wanderson O. Silva, Luis Castanheira, Laetitia Dubau, F.H. B. Lima, Carbon corrosion in proton-exchange membrane fuel cells: Spectrometric evidence for Pt-Catalysed decarboxylation at anode-relevant potentials, ChemPhysChem 20 (2019) 3106–3111.
[40] Sang Gu Ji, Haesol Kim, Hee Lee Woong, Hyung-Suk Oh, C.H. Choi, Real-time monitoring of electrochemical carbon corrosion in alkaline media, J. Mater. Chem. A 9 (2021) 19834.
[41] D.H. Kim, S. Ringe, H. Kim, S. Kim, B. Kim, G. Bae, H.S. Oh, F. Jaouen, W. Kim, H. Kim, C.H. Choi, Selective electrochemical reduction of nitric oxide to hydroxylamine by atomically dispersed iron catalyst, Nat. Commun. 12 (1) (2021) 1856.
[42] B. Ravel, M. Newville, Athena, artemis, hephaestus: data analysis for X-ray absorption spectroscopy using IFEFFIT, J. Synchrotron Radiat. 12 (Pt 4) (2005) 537–541.